Cove-edge-induced vibrational confinement and weakened collective phonon transport in graphene nanoribbons

Fei Yin,[1,2,*] Gang Wang,[1,*] A.A. Barinov,[2] Shixian Liu,[2,†] and Ke Xu[1,‡]

[1] *College of Physical Science and Technology, Bohai University, Jinzhou, China*
[2] *Department of Thermophysics, Bauman Moscow State Technical University, Moscow 105005, Russia*

Periodic cove edges alter heat conduction in graphene nanoribbons in ways that are not fully captured by geometric boundary scattering. We investigate this effect using a graphene-nanoribbon-specific neuroevolution potential together with molecular dynamics, phonon Monte Carlo simulations, lattice dynamics, and full linearized phonon Boltzmann transport calculations. Cove-edged graphene nanoribbons exhibit lower thermal conductivity than pristine armchair nanoribbons over the length and width ranges considered. The conductivity reduction obtained from molecular dynamics is larger than that predicted by the semiclassical Monte Carlo model. The residual fraction is greatest at short lengths and small widths, whereas the Monte Carlo boundary contribution becomes relatively more important as either dimension increases. Participation ratios and real-space eigenvectors identify partially confined and strongly edge-confined modes in the low- and intermediate-frequency ranges. The cove-edged ribbons also show a smaller full-LBTE correction to the relaxation-time approximation and a lower transport-weighted Normal-to-Umklapp scattering-rate ratio. These results indicate that cove-edge patterning changes both the vibrational eigenstates and the intrinsic scattering balance, thereby reducing the mode-coupling correction beyond the independent-mode approximation.

Keywords: Graphene nanoribbons; thermal conductivity; edge-confined vibrational modes; collective phonon transport; Normal and Umklapp processes; neuroevolution potential

I. INTRODUCTION

Controlling heat conduction in low-dimensional materials requires understanding not only the magnitude of thermal conductivity but also the microscopic mechanisms through which phonons transport energy. Graphene nanoribbons (GNRs) provide a representative platform for this purpose because their thermal and electronic properties can be strongly tailored through lateral confinement and atomic edge engineering [1–4]. In pristine graphene, heat is predominantly carried by low-frequency acoustic phonons with long mean free paths [5–7]. Once graphene is patterned into nanoribbons, however, atomic-scale edge morphology becomes a decisive factor governing phonon propagation. Atomically sharp edges, reconstructed boundary units, edge roughness, and nanopatterned pores can introduce phonon-boundary scattering, modify the vibrational spectrum, and generate spatially confined vibrational states [8–16]. Previous studies have therefore interpreted edge-induced reductions in thermal conductivity mainly in terms of additional boundary resistance and the suppression of efficiently propagating phonon modes. Whether an atomically structured edge can also modify the intrinsic phonon collision landscape and the collective character of heat transport remains much less understood.

This question is particularly important for systems in which momentum-conserving Normal (N) processes produce an appreciable collective correction beyond the conventional independent-mode relaxation-time approximation (RTA). When N processes dominate over momentum-relaxing Umklapp (U) processes, phonons do not relax independently but can become strongly coupled through the collision operator, giving rise to collective and hydrodynamic-like contributions to heat conduction [17–21]. Such behavior has been actively investigated in high-quality low-dimensional and layered materials [22, 23]. Atomic edge modulation may influence this regime through two related mechanisms. In addition to reflecting propagating phonons at the external boundary, an atomically structured edge can reconstruct the vibrational eigenstates, alter their group velocities and spatial character, and modify the available three-phonon scattering phase space. Edge-confined vibrations may also hybridize with extended acoustic modes and change the relative importance of N and U scattering. A direct connection among atomic edge geometry, confined vibrational modes, and the collective correction retained by the full linearized phonon Boltzmann transport equation (LBTE) has not yet been systematically established for GNRs.

Cove-edged graphene nanoribbons (Cove-GNRs) provide a controlled model system for addressing this problem. Their periodically modulated edges introduce deterministic atomic-scale variations in local width and boundary orientation while preserving translational periodicity along the nanoribbon, allowing edge-induced vibrational reconstruction to be distinguished from purely stochastic roughness scattering. Carbon-backbone motifs related to Cove-GNRs have become experimentally accessible through bottom-up solution and on-surface synthetic strategies, which enable control over ribbon

* These authors contributed equally to this work.
† lyu@bmstu.ru
‡ kickhsu@gmail.com

width, edge periodicity, and chemical structure [24, 25]. Experimentally synthesized Cove-GNRs have exhibited reduced and tunable bandgaps, while the chirality and arrangement of cove and zigzag edge segments can significantly influence their carrier-transport properties [25, 26]. Related atomically precise donor–acceptor cove-edge nanoribbons have also been investigated as electron-accepting materials, highlighting their relevance to nanoscale electronic, optoelectronic, and photovoltaic applications [27]. From a thermal-transport perspective, previous studies have shown that edge disorder, lateral confinement, and boundary reconstruction can substantially reduce the thermal conductivity of GNRs [9–12, 14]. Nevertheless, the phonon heat transport of Cove-GNRs remains much less understood than their electronic properties, particularly regarding whether periodic cove-edge modulation merely increases geometric boundary resistance or also reshapes the competition between momentum-conserving and momentum-relaxing scattering. The carbon-only, unpassivated structures considered here are idealized models designed to isolate the influence of the cove-shaped carbon backbone; effects associated with chemical termination, substrates, and environmental interactions are beyond the scope of the present work.

Resolving this issue requires a framework capable of describing both finite-size heat conduction and mode-resolved anharmonic phonon scattering in nanoribbons with relatively large and structurally complex unit cells. First-principles lattice dynamics combined with the phonon Boltzmann transport equation provides direct access to phonon dispersions, lifetimes, scattering channels, and lattice thermal conductivity [28–30]. Its direct application to Cove-GNRs, however, is computationally demanding because the extraction of high-order interatomic force constants rapidly becomes prohibitive as the unit-cell size and edge complexity increase [31, 32]. Molecular dynamics can access substantially larger spatial and temporal scales but does not directly separate mode-specific N and U scattering or resolve the collective correction contained in the full phonon collision operator. Semiclassical phonon Monte Carlo simulations can provide a controlled description of particle-like geometric boundary scattering, but they do not explicitly capture the reconstruction of vibrational eigenstates caused by the cove geometry. Machine-learning interatomic potentials, particularly the neuroevolution potential (NEP) [33, 34], bridge these descriptions by providing near-first-principles accuracy at a computational cost compatible with large-scale molecular dynamics, force-constant extraction, lattice-dynamics analysis, and full phonon Boltzmann transport calculations.

In this work, we construct a GNR-specific NEP by fine-tuning the pretrained NEP89 potential [35] using additional structures containing armchair, zigzag, and cove-shaped edge environments. Molecular-dynamics and phonon Monte Carlo results are compared to determine how much of the cove-edge-induced conductivity reduction is reproduced by geometric boundary scattering. Participation ratios and real-space eigenvectors are used to characterize the resulting vibrational modes, while full-LBTE and RTA conductivities, together with transport-weighted N and U scattering rates, are used to assess the correction arising from mode-to-mode coupling. The calculations show that cove-edge patterning lowers the thermal conductivity, produces edge-confined vibrational modes, and reduces both the Normal-to-Umklapp scattering-rate ratio and the full-LBTE correction beyond the RTA description.

II. METHODOLOGY

A. Construction of the NEP-GNRs potential

A graphene-nanoribbon-specific neuroevolution potential, denoted as NEP-GNRs, was constructed by fine-tuning the pretrained NEP89 model [35]. The additional dataset contained monolayer graphene nanoribbons with armchair, zigzag, and cove-shaped edges, different ribbon widths, and locally perturbed atomic environments. Random atomic displacements of approximately 0.01–0.05 Å were applied to the initial structures to sample local distortions associated with different edge configurations.

All nanoribbon models considered in this work were carbon-only structures with unpassivated edges. The same edge-termination convention was used for the AGNR and Cove-GNR systems so that their differences originate from the carbon-backbone geometry rather than from different chemical terminations. The present models therefore isolate the intrinsic influence of cove-edge patterning on phonon transport; the effects of hydrogen passivation, functional groups, substrates, and environmental interactions are beyond the scope of this work. All structures were fully relaxed before the molecular-dynamics, lattice-dynamics, and phonon-transport calculations.

To further enrich the dataset with finite-temperature structural perturbations, short ab initio molecular dynamics simulations were performed for two representative GNR structures at 300 K. The AIMD simulations employed a time step of 0.5 fs and contained 100 ionic steps, corresponding to a total duration of 50 fs. Twenty configurations were uniformly extracted from each trajectory, yielding 40 AIMD configurations. These short trajectories were used to introduce thermally perturbed local environments into the fine-tuning dataset rather than to provide statistically converged finite-temperature sampling. Configurations from the datasets of Wang et al. [36] and Liang et al. [37] were also incorporated after consistency checks and removal of structures with unphysical local geometries or anomalous reference values. The final fine-tuning dataset contained 713 configurations.

Reference energies, atomic forces, and virial components were calculated using density functional theory

as implemented in VASP. The Perdew–Burke–Ernzerhof exchange–correlation functional, a plane-wave cutoff energy of 600 eV, and an automatic k-point sampling scheme with `KSPACING = 0.20` Å^{-1} were employed. The electronic convergence criterion was set to 10^{-6} eV. The detailed AIMD and single-point DFT input settings are provided in Sections S1 and S2 of the Supplementary Information.

The pretrained NEP89 model was fine-tuned using GPUMD for 20,000 generations, with checkpoint potentials saved every 2,000 generations. The predicted thermal conductivity reached a stable plateau after approximately 18,000 generations, and the corresponding checkpoint potential was therefore selected for the subsequent calculations. The same NEP-GNRs model was used consistently for molecular dynamics simulations, force-constant fitting, lattice-dynamics calculations, and phonon Boltzmann transport calculations. The complete fine-tuning input and hyperparameters are provided in Section S3 of the Supplementary Information.

B. Molecular-dynamics thermal transport calculations

The length-dependent thermal conductivity was calculated at 300 K using a spectral reconstruction method combining homogeneous nonequilibrium molecular dynamics (HNEMD) with the NEMD-based spectral heat-current method. The diffusive spectral thermal conductivity, $\kappa_{\mathrm{diff}}(\omega)$, was obtained from HNEMD simulations, whereas the spectral ballistic conductance, $G(\omega)$, was evaluated from NEMD simulations. Their ratio defines the frequency-dependent phonon mean free path,

$$\lambda(\omega) = \frac{\kappa_{\mathrm{diff}}(\omega)}{G(\omega)}. \tag{1}$$

The thermal conductivity of a nanoribbon with transport length L was then reconstructed as

$$\kappa_{\mathrm{MD}}(L) = \int_0^\infty \frac{d\omega}{2\pi} \frac{\kappa_{\mathrm{diff}}(\omega)}{1 + \lambda(\omega)/L}. \tag{2}$$

Throughout this work, the ribbon width W was defined as the minimum transverse distance between the two opposing edges. The AGNR and Cove-GNR compared at each data point were constructed with the same minimum width. Because the local width of the Cove-GNR varies periodically along the transport direction, W represents its bottleneck width rather than its spatially averaged width. The same effective thickness, $t = 0.335$ nm, was used in the MD and MC calculations, and the nominal cross-sectional area was defined as $A = Wt$ for both edge geometries.

C. Phonon Monte Carlo simulations and residual thermal suppression

Phonon Monte Carlo simulations were performed at 300 K as a complementary semiclassical model for evaluating the thermal-conductivity reduction caused by geometric boundary scattering. To isolate the influence of boundary geometry, the same mode-resolved phonon properties of pristine graphene, including the phonon frequencies, group velocities, relaxation times, and mode heat capacities, were used for both AGNR and Cove-GNR simulations. Consequently, the difference between their Monte Carlo thermal conductivities originates from the different boundary geometries rather than from edge-induced changes in the intrinsic phonon spectrum or phonon–phonon scattering rates.

Phonon particles were characterized by their mode index $\lambda = (\mathbf{q}, s)$, angular frequency ω_λ, group velocity $\mathbf{v}_\lambda$, relaxation time τ_λ, and mode heat capacity. Intrinsic phonon scattering was treated within the relaxation-time approximation. The probability that a phonon in mode λ undergoes intrinsic scattering during a time interval Δt was calculated as

$$P_\lambda^{\mathrm{int}} = 1 - \exp\left(-\frac{\Delta t}{\tau_\lambda}\right). \tag{3}$$

Each simulation employed 2.0×10^5 computational phonon particles and was advanced for 5.0×10^4 time steps with $\Delta t = 0.005$ ns, corresponding to a total simulated duration of 250 ns.

For AGNRs, the lateral boundaries were represented by straight ribbon edges, whereas the periodically modulated cove-shaped profile was explicitly incorporated into the Cove-GNR geometry. At each boundary collision, the probability of specular reflection was determined using the Ziman–Soffer relation,

$$p_{\mathrm{spec}} = \exp\left[-4\eta^2 k^2 \cos^2\theta\right], \tag{4}$$

where $\eta = 0.1$ nm is the boundary roughness parameter, k is the magnitude of the incident phonon wave vector, and θ is the angle between the incident wave vector and the local boundary normal. The deterministic cove-shaped boundary profile was explicitly resolved in the MC geometry. The parameter $\eta = 0.1$ nm therefore does not represent the cove modulation itself, but phenomenologically accounts for unresolved atomic-scale deviations from the idealized boundary profile. The same roughness parameter was used for the AGNR and Cove-GNR calculations so that their difference remained primarily associated with the deterministic boundary geometry. Diffuse reflection was applied with probability $1 - p_{\mathrm{spec}}$. Following a diffuse boundary event, the outgoing phonon mode was resampled from the allowed modes propagating back into the computational domain.

Because the MC model uses the same pristine-graphene phonon properties for both edge geometries and treats phonons as semiclassical propagating particles, it captures intrinsic relaxation, finite-size transport,

and geometric boundary reflection but does not explicitly include the reconstruction of vibrational eigenstates caused by cove-edge patterning. The MC results therefore provide a controlled reference for the conductivity suppression expected from particle-like boundary scattering.

The total edge-induced conductivity reduction obtained from molecular dynamics and the corresponding semiclassical boundary-scattering contribution were defined as

$$\Delta\kappa_{\mathrm{total}} = \kappa_{\mathrm{MD}}^{\mathrm{AGNR}} - \kappa_{\mathrm{MD}}^{\mathrm{Cove}}, \tag{5}$$

$$\Delta\kappa_{\mathrm{bd}} = \kappa_{\mathrm{MC}}^{\mathrm{AGNR}} - \kappa_{\mathrm{MC}}^{\mathrm{Cove}}. \tag{6}$$

The residual suppression beyond the semiclassical boundary-scattering model was then evaluated as

$$\Delta\kappa_{\mathrm{res}} = \Delta\kappa_{\mathrm{total}} - \Delta\kappa_{\mathrm{bd}}, \tag{7}$$

and the corresponding relative fractions were calculated from

$$\eta_{\mathrm{bd}} = \frac{\Delta\kappa_{\mathrm{bd}}}{\Delta\kappa_{\mathrm{total}}}, \qquad \eta_{\mathrm{res}} = \frac{\Delta\kappa_{\mathrm{res}}}{\Delta\kappa_{\mathrm{total}}}. \tag{8}$$

Here, $\Delta\kappa_{\mathrm{res}}$ is an operational measure of the conductivity suppression not captured by the semiclassical geometric-boundary model, rather than a uniquely separable localization contribution. Vibrational features that are absent from the MC model are examined separately through participation-ratio and real-space eigenmode analyses.

D. Lattice dynamics and phonon Boltzmann transport calculations

Harmonic and third-order interatomic force constants were obtained using the NEP-GNRs potential through the NEP-kappa workflow [32]. Before force-constant generation, each structure was relaxed using the trained potential. A $4 \times 1 \times 1$ supercell was employed, and 500 randomly displaced structures were generated with a displacement standard deviation of 0.01 Å and a minimum interatomic distance of 1.1 Å. The cutoff radii for the second- and third-order force constants were 7.0 and 6.0 Å, respectively. The force constants were fitted using hiPhive, and the phonon transport properties were calculated on a $51 \times 1 \times 1$ wave-vector mesh over the temperature range from 100 to 1000 K in steps of 100 K. The complete NEP-kappa input parameters are provided in Section S4 of the Supplementary Information.

The lattice thermal conductivity was calculated using Phono3py under both the relaxation-time approximation and the direct solution of the full linearized phonon Boltzmann transport equation following the method of Chaput [30, 38]. Because the nanoribbon simulation cells contain vacuum in the nonperiodic directions, the RTA and full-LBTE thermal conductivities were renormalized by the factor $A_{\mathrm{cell}}/(Wt)$, where A_{cell} is the total simulation-cell cross-sectional area including vacuum, W is the minimum ribbon width, and $t = 0.335$ nm is the effective graphene thickness. Isotope scattering was not included, and the collision operator therefore contained intrinsic three-phonon scattering processes only. The RTA neglects the off-diagonal coupling of the phonon collision operator and treats each phonon mode as relaxing independently, whereas the full-LBTE solution retains the mode-to-mode coupling contained in the three-phonon collision matrix.

Recent first-principles analysis has shown that the ratio $\kappa_{\mathrm{LBTE}}/\kappa_{\mathrm{RTA}}$ can serve as an indicator of collective and hydrodynamic phonon-transport signatures [39]. Here, we use the following equivalent monotonic measure of the correction beyond the independent-mode RTA description:

$$\eta_{\mathrm{LBTE}} = \frac{\kappa_{\mathrm{LBTE}} - \kappa_{\mathrm{RTA}}}{\kappa_{\mathrm{LBTE}}} = 1 - \frac{\kappa_{\mathrm{RTA}}}{\kappa_{\mathrm{LBTE}}}. \tag{9}$$

The quantity η_{LBTE} is used as an indicator of the collective correction arising from mode-to-mode coupling rather than as a strictly separable fraction of the total thermal conductivity. A larger η_{LBTE} corresponds to a stronger full-LBTE enhancement relative to the RTA prediction.

Three-phonon scattering processes were decomposed into Normal and Umklapp contributions according to crystal-momentum conservation,

$$\mathbf{q}_1 \pm \mathbf{q}_2 - \mathbf{q}_3 = \mathbf{G}, \tag{10}$$

where processes with $\mathbf{G} = \mathbf{0}$ were classified as Normal processes and those with $\mathbf{G} \neq \mathbf{0}$ as Umklapp processes. To minimize representation-dependent differences in the Normal/Umklapp classification, the AGNR and Cove-GNR structures were represented using the same axial periodicity and reciprocal-lattice convention when their scattering processes were compared.

To emphasize phonon modes with larger heat-capacity and group-velocity weights, the Normal and Umklapp scattering rates were averaged using the factor $C_\lambda|\mathbf{v}_\lambda|^2$. The transport-weighted average scattering rate was defined as

$$\langle\Gamma_X\rangle = \frac{\sum_\lambda C_\lambda \left|\mathbf{v}_\lambda\right|^2 \Gamma_{X,\lambda}}{\sum_\lambda C_\lambda \left|\mathbf{v}_\lambda\right|^2}, \qquad X = N, U, \tag{11}$$

where C_λ and $\mathbf{v}_\lambda$ are the heat capacity and group velocity of phonon mode λ, respectively, and $\Gamma_{N,\lambda}$ and $\Gamma_{U,\lambda}$ are its Normal and Umklapp three-phonon scattering rates. The corresponding transport-weighted Normal-to-Umklapp ratio was defined as $\langle\Gamma_N\rangle/\langle\Gamma_U\rangle$. This ratio characterizes the relative predominance of momentum-conserving and momentum-relaxing scattering among phonon modes with larger heat-capacity and group-velocity weights. Because this ratio alone does not

uniquely determine collective transport, it was interpreted together with the difference between the full-LBTE and RTA thermal conductivities.

The spatial character of each phonon mode was quantified using the participation ratio,

$$P(\mathbf{q},s)=\frac{\left[\sum_i\sum_\alpha |e_{i\alpha}(\mathbf{q},s)|^2\right]^2}{N\sum_i\left(\sum_\alpha |e_{i\alpha}(\mathbf{q},s)|^2\right)^2}, \tag{12}$$

where N is the number of atoms in the unit cell and $e_{i\alpha}(\mathbf{q},s)$ is the normalized eigenvector component of atom i along Cartesian direction α. Values close to unity correspond to modes extended throughout the unit cell, whereas smaller values indicate vibrations confined to a smaller subset of atoms. The participation ratios were analyzed together with real-space eigenvectors to distinguish extended, partially confined, and strongly edge-confined vibrational modes.

III. RESULTS AND DISCUSSION

A. Validation of the NEP-GNRs potential

Because the same NEP-GNRs potential was used for molecular dynamics simulations, force-constant fitting, lattice-dynamics analysis, and phonon Boltzmann transport calculations, its reliability must be assessed at several complementary levels. We therefore examined the structural coverage of the training dataset, the accuracy of the predicted energetics and harmonic phonon properties, and the stability of the calculated thermal conductivity during fine-tuning.

Figure 1(a) shows a principal component analysis (PCA) projection of the atomic descriptors included in the fine-tuning dataset. The configurations span a broad region of descriptor space and cover local environments associated with pristine graphene-like structures, armchair and zigzag edges, cove-shaped boundaries, and thermally or randomly perturbed configurations. This structural diversity is important because the local coordination and bonding environments near reconstructed edges differ appreciably from those in bulk-like graphene. The PCA distribution therefore indicates that the fine-tuning dataset provides relevant coverage of both interior and edge atomic environments encountered in the subsequent AGNR and Cove-GNR calculations.

The harmonic accuracy of the potential is evaluated in Fig. 1(b) by comparing the phonon dispersion of pristine graphene predicted by NEP-GNRs with the corresponding DFT result. The NEP-GNRs dispersion reproduces the overall acoustic and optical branch structure and follows the reference DFT frequencies over the sampled Brillouin-zone path. In particular, the agreement in the low-frequency acoustic branches is important for thermal-transport calculations because these modes make a substantial contribution to heat conduction. This comparison indicates that the fine-tuned potential reproduces the main harmonic features underlying the phonon frequencies and group velocities of pristine graphene.

Figure 1(c) evaluates the energetic accuracy of NEP-GNRs for the configurations included in the parity analysis. The predicted energies closely follow the DFT reference values over the full energy range, with an MAE of approximately 27.0 meV atom^{-1} and an RMSE of approximately 34.0 meV atom^{-1}. The absence of pronounced systematic deviations indicates that the potential consistently describes configurations containing both graphene-like interior environments and reconstructed edge structures. Together with the phonon-dispersion comparison, the energetic agreement supports the use of NEP-GNRs for simulations involving structural perturbations and vibrational dynamics in graphene nanoribbons.

The convergence of the fine-tuning process was further assessed through the calculated thermal conductivity, as shown in Fig. 1(d). Starting from the pretrained NEP89 model, the predicted thermal conductivity changes rapidly during the early stages of fine-tuning and subsequently reaches a stable plateau. Beyond approximately 18,000 generations, further training produces no appreciable variation in the calculated conductivity. The value obtained from the converged model also falls within the range of representative first-principles and experimental results reported for graphene, although the literature values span a broad interval because of differences in sample size, isotope composition, defect concentration, and measurement or simulation conditions. The checkpoint obtained after 18,000 generations was therefore selected for the subsequent calculations. These validation results support the use of the NEP-GNRs potential for the structural, vibrational, and thermal-transport calculations performed in this work.

B. Size-dependent thermal conductivity and residual edge-induced suppression

The atomic structures considered in this work are shown in Figs. 2(a) and 2(b). A pristine carbon-only AGNR with straight, periodic, and unpassivated armchair edges serves as the reference structure, whereas the carbon-only Cove-GNR contains periodically modulated unpassivated cove-shaped boundaries. Here, "pristine AGNR" refers to the ideal straight-edged nanoribbon without cove modulation, additional edge disorder, or chemical functionalization. The same edge-termination convention is used for both systems, allowing the effect of the carbon-backbone geometry to be isolated from that of chemical passivation. Compared with the straight armchair edge, the cove geometry introduces deterministic atomic-scale variations in the local width and boundary orientation.

Figure 2(c) compares the length-dependent thermal conductivity obtained from the MD-based spectral recon-

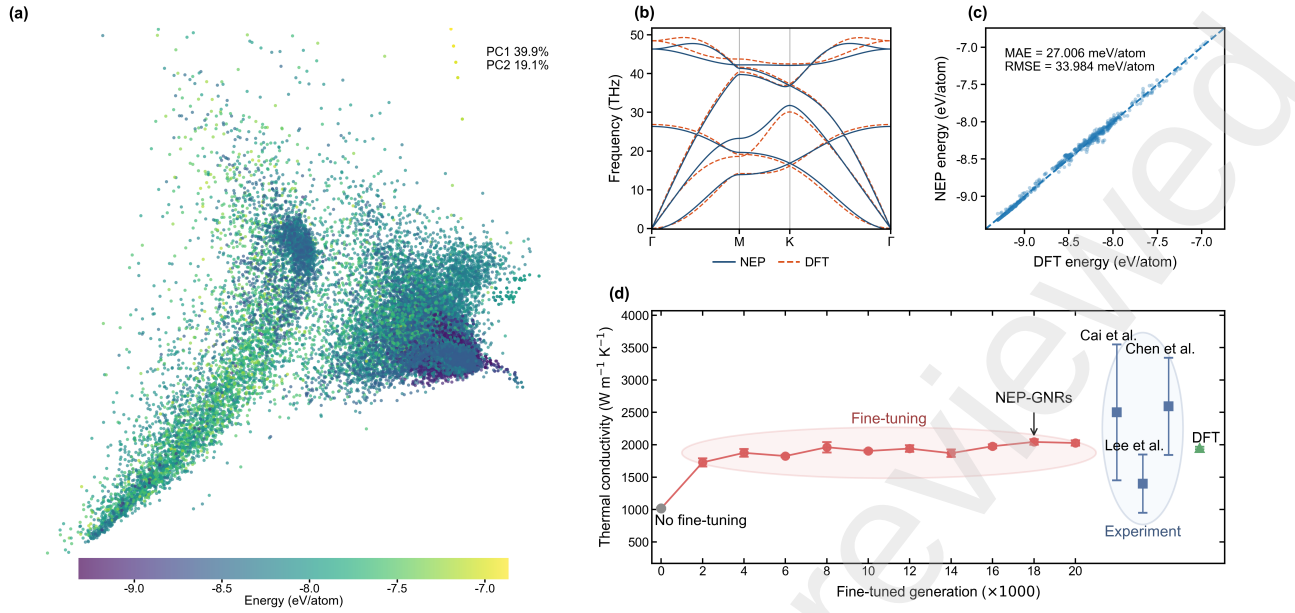

FIG. 1. Validation of the fine-tuned NEP-GNRs potential. (a) Principal component analysis projection of the atomic descriptors in the fine-tuning dataset. (b) Phonon dispersion of pristine graphene predicted by NEP-GNRs compared with the reference DFT result along the Γ–M–K–Γ path. (c) Parity plot comparing the energies predicted by NEP-GNRs with the corresponding DFT reference values. MAE and RMSE denote the mean absolute error and root-mean-square error, respectively. (d) Evolution of the predicted thermal conductivity of pristine graphene at 300 K during fine-tuning from the pretrained NEP89 model to NEP-GNRs, together with representative DFT and experimental values reported in the literature [40–42].

struction and phonon MC simulations at a fixed width of $W = 20$ nm. For qualitative comparison, room-temperature experimental data points for suspended graphene reported by Xu et al. are also included [43]. Both the measurements and the present calculations exhibit a monotonic increase in thermal conductivity with transport length. The experimental data thus provide a qualitative reference for the predicted length dependence.

In all calculated cases, the thermal conductivity increases with transport length as phonons with progressively longer mean free paths contribute to heat conduction. Cove-GNRs exhibit lower thermal conductivity than pristine AGNRs over the entire length range considered, demonstrating that the periodically modulated edge strongly suppresses heat conduction. The difference between the two structures also becomes more pronounced with increasing length. Whereas the conductivity of the AGNR continues to increase substantially, the corresponding growth in the Cove-GNR is weaker. This weaker length dependence is consistent with stronger suppression of transport channels associated with relatively long phonon mean free paths.

The comparison between MD and MC provides further information about the physical origin of this reduction. In the MC calculations, both AGNRs and Cove-GNRs were assigned the same mode-resolved phonon properties of pristine graphene, so their conductivity difference arises exclusively from the different geometric boundaries and the associated semiclassical phonon reflection. The MD simulations, in contrast, explicitly describe the atomistic vibrational dynamics of each nanoribbon and therefore include edge-induced changes in the vibrational spectrum, anharmonic interactions, and mode hybridization. The larger conductivity reduction obtained from MD shows that geometric boundary reflection alone is insufficient to reproduce the full influence of the cove edge.

The model-based comparison in Fig. 2(d) quantifies this difference. The total conductivity reduction, $\Delta\kappa_{\mathrm{total}}$, increases with ribbon length, indicating that the effect of the cove geometry becomes more pronounced as longer-mean-free-path phonons contribute to transport. The semiclassical boundary-scattering contribution, $\Delta\kappa_{\mathrm{bd}}$, also increases with length and becomes the largest absolute component in sufficiently long nanoribbons. By comparison, the residual suppression, $\Delta\kappa_{\mathrm{res}}$, increases more moderately and tends toward saturation.

Here, $\Delta\kappa_{\mathrm{res}}$ is an operational residual defined by the difference between the MD and MC reductions. Because the two approaches differ in their physical descriptions, it cannot be assigned uniquely to a single microscopic mechanism. The participation-ratio and eigenmode analyses below examine vibrational features that are absent from the semiclassical MC model.

The relative fractions in Fig. 2(e) further illustrate the length-dependent crossover. At short lengths, the residual fraction η_{res} constitutes the larger part of the total conductivity reduction, whereas the boundary-scattering fraction η_{bd} is relatively small. As the ribbon length increases, η_{bd} rises and η_{res} decreases. This trend shows that the relative importance of suppression not captured

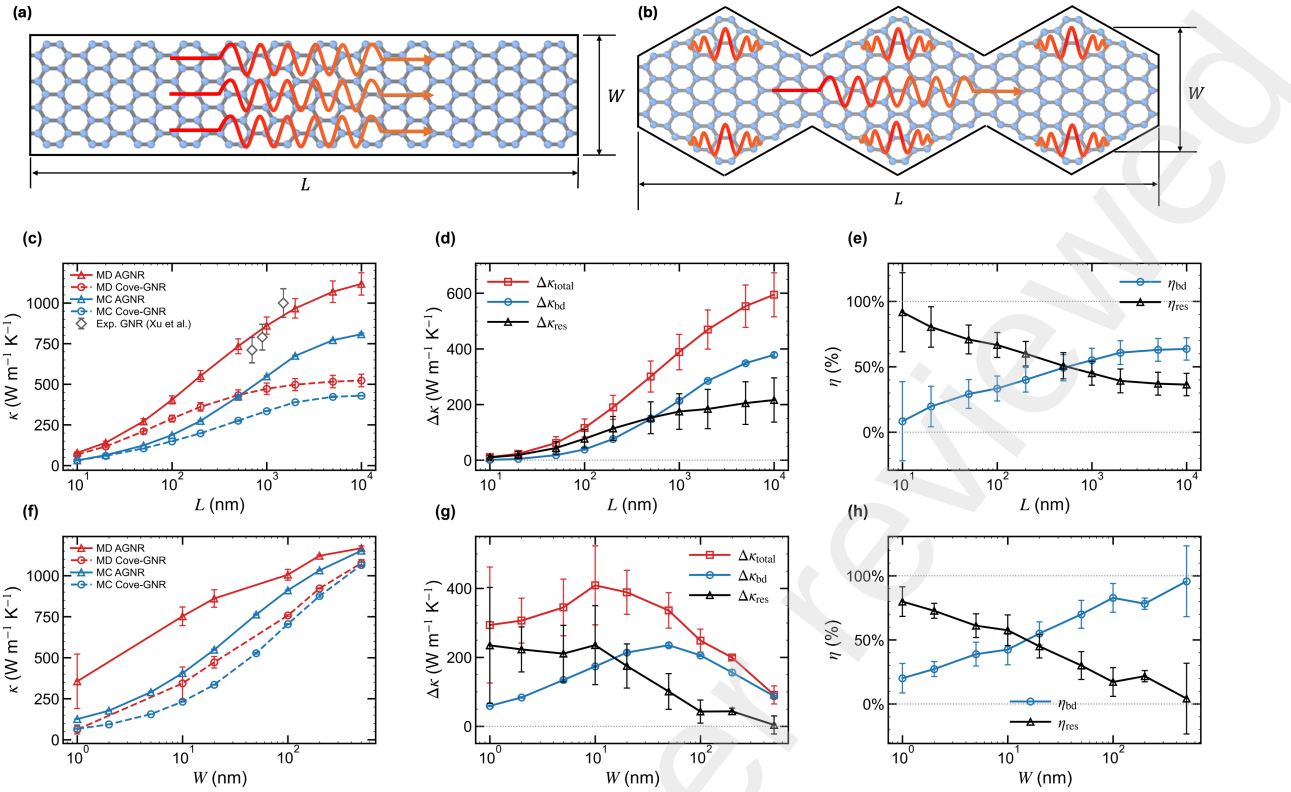

FIG. 2. Atomic structures and size-dependent thermal-transport suppression in graphene nanoribbons with different edge morphologies. (a) Pristine carbon-only AGNR with unpassivated straight armchair edges. (b) Carbon-only Cove-GNR with unpassivated periodically modulated edges. Here, W denotes the minimum transverse distance between the two opposing edges, and the AGNR and Cove-GNR are compared at the same W. (c) Length-dependent thermal conductivity κ at a fixed width of $W = 20$ nm obtained from MD-based spectral reconstruction and phonon MC simulations. Gray open diamonds denote room-temperature experimental data for suspended graphene reported by Xu et al. [43]. (d) Length-dependent comparison of the total MD reduction $\Delta\kappa_{\mathrm{total}}$, the boundary reduction predicted by the semiclassical MC model $\Delta\kappa_{\mathrm{bd}}$, and the resulting model residual $\Delta\kappa_{\mathrm{res}}$. (e) Corresponding normalized model terms η_{bd} and η_{res} as functions of length. (f) Width-dependent thermal conductivity at a fixed length of $L = 1000$ nm. (g) Corresponding width-dependent comparison of $\Delta\kappa_{\mathrm{total}}$, $\Delta\kappa_{\mathrm{bd}}$, and $\Delta\kappa_{\mathrm{res}}$. (h) Normalized model terms η_{bd} and η_{res} as functions of width. In panels (c) and (f), red and blue curves denote the MD and MC results, respectively; solid triangle-marked lines correspond to pristine AGNRs, whereas dashed circle-marked lines correspond to Cove-GNRs. The experimental data in panel (c) are included only as a qualitative reference for the length-dependent trend because the measured samples were much wider suspended graphene structures rather than atomically precise nanoribbons.

by the semiclassical boundary model is greatest in short nanoribbons, while the semiclassical boundary term accounts for an increasing fraction of the total conductivity reduction as the transport length grows.

Figures 2(f)–2(h) show the corresponding width-dependent results at a fixed length of $L = 1000$ nm. The thermal conductivity increases with ribbon width for both AGNRs and Cove-GNRs as the boundary-to-interior ratio decreases and the relative influence of the edges becomes weaker. Nevertheless, the conductivity of the Cove-GNR remains lower than that of the AGNR throughout the studied width range, indicating that the influence of the periodically modulated edge is not restricted to the narrowest structures.

Figures 2(g) and 2(h) quantify the width dependence of the conductivity reduction and its normalized components. The total reduction, $\Delta\kappa_{\mathrm{total}}$, decreases as the ribbon becomes wider. The residual suppression, $\Delta\kappa_{\mathrm{res}}$, is most pronounced in the narrowest ribbons and decreases with increasing width, whereas the semiclassical boundary contribution, $\Delta\kappa_{\mathrm{bd}}$, remains appreciable over a broader width range.

The normalized terms reveal the corresponding crossover. In narrow nanoribbons, η_{res} exceeds η_{bd}, indicating that most of the conductivity reduction is not reproduced by the semiclassical geometric-boundary model. With increasing width, η_{res} decreases, while η_{bd} increases and eventually becomes dominant. Together with the length-dependent results, the MD–MC comparison shows that the relative model residual is largest at short lengths and small widths, whereas the geometric boundary term accounts for an increasing fraction of the total reduction as either dimension increases.

C. Edge-confined vibrational modes in Cove-GNRs

To examine vibrational features that are absent from the semiclassical boundary model, we analyze the phonon dispersions, participation ratios, and representative real-space eigenvectors of the AGNR and Cove-GNR. The participation ratio measures the fraction of atoms involved in a phonon mode: values close to unity correspond to vibrations distributed throughout the unit cell, whereas smaller values indicate that the atomic displacements are concentrated on a smaller subset of atoms. Because the modes retain a well-defined wave vector along the periodic direction, a reduced participation ratio is interpreted as spatial confinement within the nanoribbon unit cell rather than complete localization along the transport direction.

Figure 3(a) compares the frequency-resolved average participation ratios of the two nanoribbons. The pristine AGNR maintains relatively large participation ratios over a broad frequency range, including the low-frequency region containing acoustic branches. In contrast, the Cove-GNR exhibits lower participation ratios within several low- and intermediate-frequency intervals, showing that the periodic edge modulation changes the spatial distribution of its vibrational eigenstates.

The mode-resolved dispersions in Figs. 3(b) and 3(c) provide a more detailed comparison. Many low-frequency branches in the AGNR retain large participation ratios, indicating displacement fields that extend across most of the ribbon. The Cove-GNR contains more branches with reduced participation ratios, particularly in the low- and intermediate-frequency regions. These branches indicate stronger spatial confinement, while their specific edge-centered character is examined below using representative real-space eigenvectors.

The enlarged low-frequency region in Fig. 3(d) shows that the reduction in participation ratio extends to acoustic and low-lying branches. A reduced participation ratio does not by itself determine the longitudinal group velocity or modal thermal conductivity. It nevertheless shows that the vibrational amplitude is redistributed toward a smaller part of the nanoribbon, representing a mode-level effect that is absent from the semiclassical boundary model.

The representative eigenvectors in Figs. 3(e)–3(g) illustrate three different spatial distributions. The mode in Fig. 3(e), with PR = 0.996316, has an almost uniform displacement field across the nanoribbon and is therefore identified as an extended mode.

The mode in Fig. 3(f) has an intermediate participation ratio of PR = 0.611043. Its displacement field spans a substantial part of the ribbon but is more unevenly distributed, with enhanced motion in selected edge regions. We therefore describe this mode as partially confined rather than fully localized.

For the mode in Fig. 3(g), the participation ratio decreases to PR = 0.143395. Most of its vibrational amplitude is concentrated on atoms near the cove-shaped boundaries, while the ribbon interior participates only weakly. This displacement pattern identifies the mode as strongly edge-confined. The real-space eigenvector is essential for this classification because a small participation ratio alone does not specify where the vibrational amplitude is located.

The participation ratios and real-space eigenvectors show that the cove geometry produces modes with different degrees of spatial confinement, including strongly edge-confined modes in the low- and intermediate-frequency ranges. The cove boundary therefore changes the vibrational eigenstates rather than acting solely as a geometric reflecting surface.

D. Reduced collective correction in Cove-GNRs

We next examine whether cove-edge patterning changes the correction beyond the independent-mode RTA description. The second- and third-order interatomic force constants were obtained through the NEP-kappa workflow [32] using the same NEP-GNRs potential as in the molecular-dynamics calculations. The lattice-dynamics, scattering-rate, and Boltzmann transport calculations are therefore based on a common description of the interatomic interactions.

Figures 4(a) and 4(b) compare the temperature-dependent RTA and full-LBTE thermal conductivities of the AGNRs and Cove-GNRs. For the AGNRs, the full-LBTE conductivity is consistently higher than the RTA result, particularly at lower temperatures. Because the RTA neglects the off-diagonal coupling of the collision operator, the difference between the two solutions reflects the correction arising from mode-to-mode coupling.

For the Cove-GNRs, the difference between the full-LBTE and RTA conductivities is substantially smaller than that in the corresponding AGNRs. The same trend is found for both ribbon widths. Figure 4(c) shows that Cove-GNRs have smaller values of η_{LBTE} over the temperature range considered, indicating a reduced correction beyond the independent-mode RTA description. This difference should not be interpreted as a ballistic-to-diffusive transition; it reflects a weaker contribution from the mode-to-mode coupling retained by the full collision operator.

To examine the scattering processes associated with this trend, the intrinsic three-phonon rates were separated into Normal and Umklapp contributions. Normal processes conserve crystal momentum within the first Brillouin zone, whereas Umklapp processes involve a nonzero reciprocal-lattice vector and relax crystal momentum. The AGNR and Cove-GNR were represented using the same axial periodicity and reciprocal-lattice convention to reduce representation-dependent differences in the Normal/Umklapp classification.

Figures 4(d) and 4(e) show the mode-resolved Normal and Umklapp scattering rates of the 1-nm-wide AGNR at 100 and 300 K. At 100 K, the Normal rates exceed the

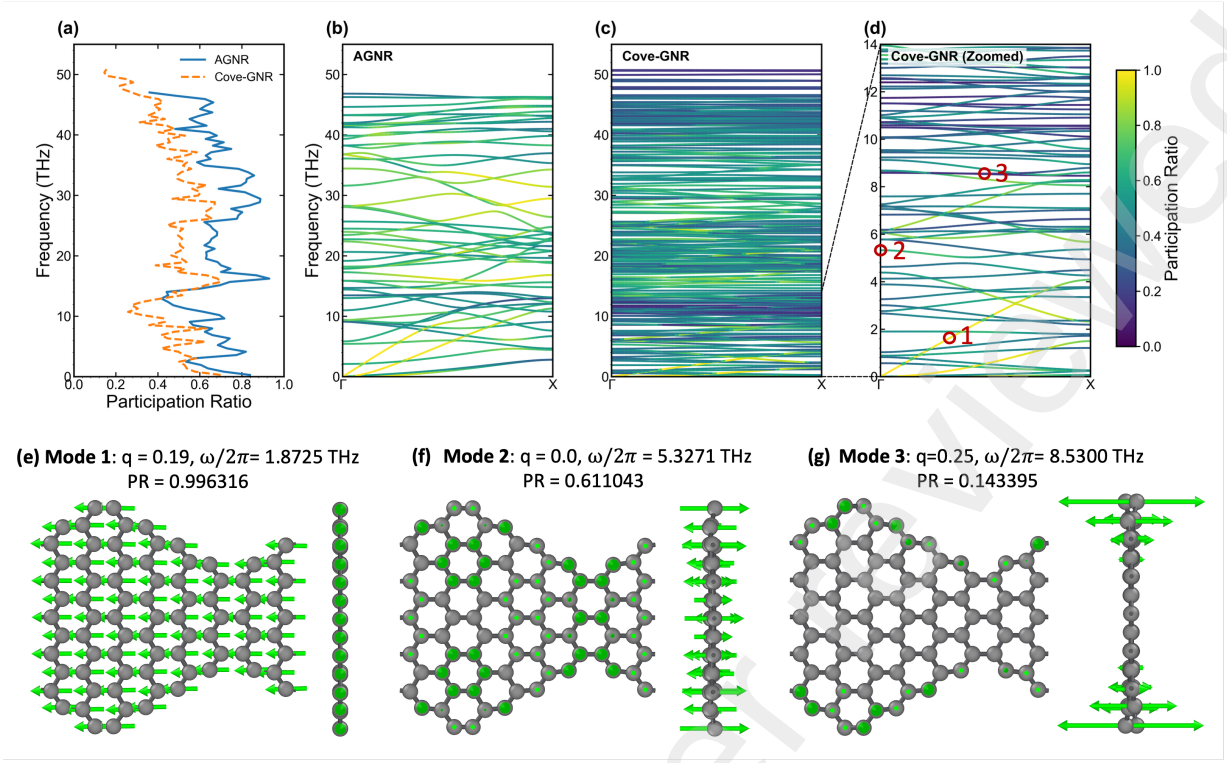

FIG. 3. Participation-ratio analysis and representative phonon eigenmodes of the AGNR and Cove-GNR. (a) Frequency-resolved average participation ratios of phonon modes in the two nanoribbons. Smaller values indicate stronger spatial confinement of the atomic displacements within the unit cell. (b) Phonon dispersion of the AGNR colored by the mode participation ratio. (c) Phonon dispersion of the Cove-GNR colored by the mode participation ratio. (d) Enlarged low-frequency region of the Cove-GNR dispersion. Red circles identify three representative modes selected for real-space eigenvector visualization. (e) Representative extended mode in the Cove-GNR at the reduced wave-vector coordinate $q = 0.19$, with $\omega/2\pi = 1.8725$ THz and PR $= 0.996316$. (f) Representative partially confined mode at the Γ point, with $q = 0$, $\omega/2\pi = 5.3271$ THz and PR $= 0.611043$. (g) Representative strongly edge-confined mode at $q = 0.25$, with $\omega/2\pi = 8.5300$ THz and PR $= 0.143395$. Green arrows represent the atomic displacement vectors. The color scale in panels (b)–(d) denotes the participation ratio, with larger values corresponding to spatially extended modes and smaller values corresponding to increasingly confined modes.

Umklapp rates over a broad part of the low-frequency spectrum. This region contains acoustic modes that contribute substantially to heat conduction, consistent with the relatively large full-LBTE correction of the AGNR. At 300 K, both rates increase, while the difference between the Normal and Umklapp contributions becomes smaller.

The transport-weighted averages in Fig. 4(f) summarize this temperature dependence. At low temperatures, $\langle\Gamma_N\rangle$ is substantially larger than $\langle\Gamma_U\rangle$. The ratio $\langle\Gamma_N\rangle/\langle\Gamma_U\rangle$ decreases with increasing temperature as the relative contribution of Umklapp scattering grows, in parallel with the reduction in η_{LBTE}.

The corresponding Cove-GNR results are shown in Figs. 4(g) and 4(h). Compared with the AGNR, the separation between the Normal and Umklapp rates is smaller over much of the low- and intermediate-frequency spectrum. The altered vibrational spectrum is therefore accompanied by a change in the intrinsic three-phonon scattering landscape, with a greater relative contribution from momentum-relaxing processes.

Figure 4(i) shows that the transport-weighted $\langle\Gamma_N\rangle/\langle\Gamma_U\rangle$ ratio of the 1-nm-wide Cove-GNR remains below that of the corresponding AGNR. Normal scattering is still important, but its predominance over Umklapp scattering is reduced. This trend is consistent with the smaller full-LBTE correction in Figs. 4(a)–4(c).

The two indicators point in the same direction: Cove-GNRs have both a smaller full-LBTE correction and a lower transport-weighted $\langle\Gamma_N\rangle/\langle\Gamma_U\rangle$ ratio. Together with the participation-ratio results, this suggests that cove-edge-induced changes in the vibrational eigenstates and scattering phase space reduce the relative role of momentum-conserving mode coupling. The cove modulation therefore affects both boundary scattering and the part of the collision dynamics omitted by the RTA.

IV. CONCLUSION

In this work, we examined phonon heat transport in cove-edged graphene nanoribbons using molecular dy-

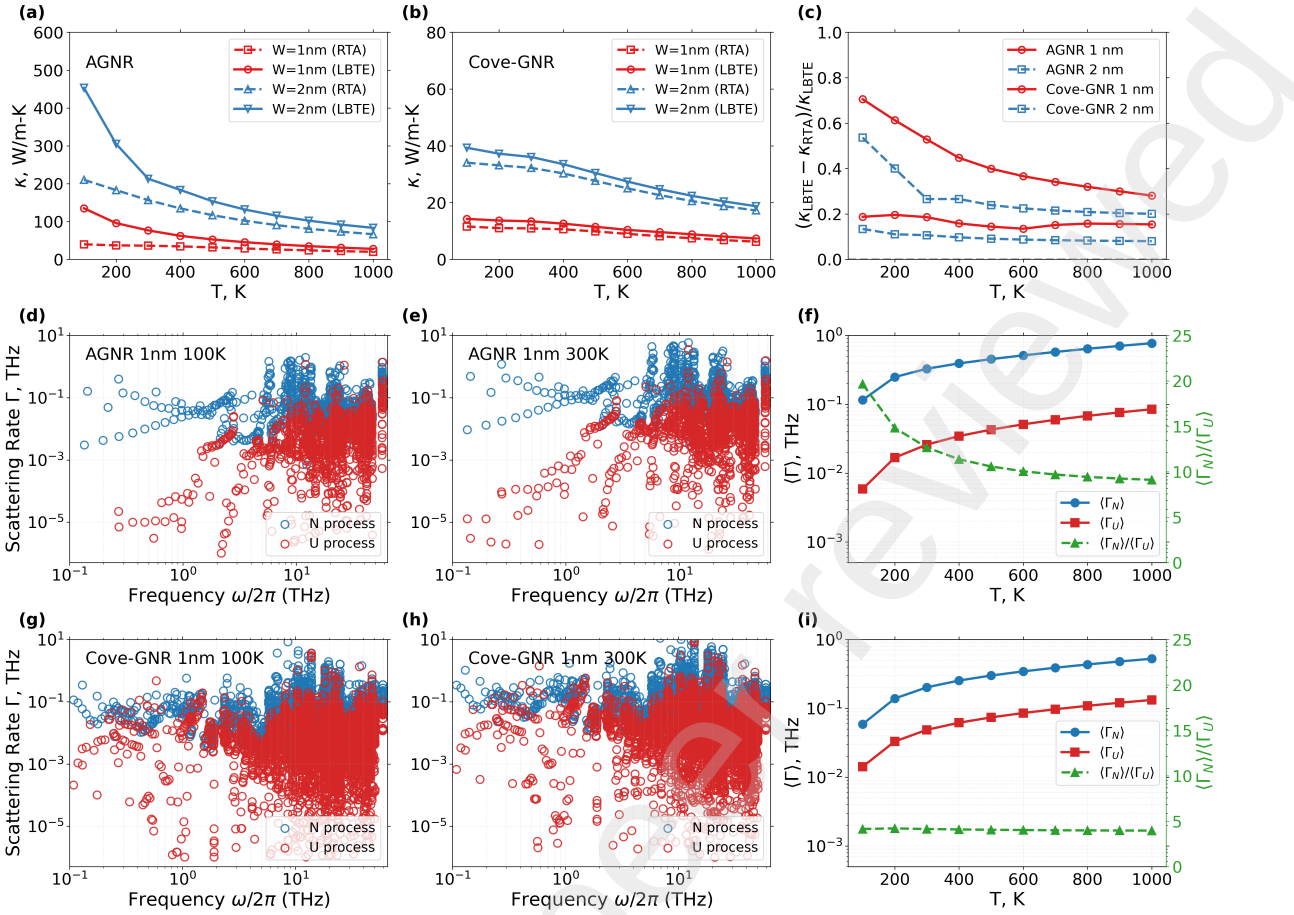

FIG. 4. Lattice thermal transport and Normal/Umklapp scattering in graphene nanoribbons with different edge geometries. (a,b) Temperature-dependent thermal conductivity κ of AGNRs and Cove-GNRs with widths of 1 and 2 nm, calculated using the relaxation-time approximation and the direct solution of the full linearized phonon Boltzmann transport equation. (c) Relative full-LBTE correction, $\eta_{\mathrm{LBTE}} = (\kappa_{\mathrm{LBTE}} - \kappa_{\mathrm{RTA}})/\kappa_{\mathrm{LBTE}}$, used as an indicator of the correction beyond the independent-mode RTA description. (d,e) Frequency-dependent Normal (N) and Umklapp (U) three-phonon scattering rates in the 1-nm-wide AGNR at 100 and 300 K, respectively. (f) Transport-weighted average scattering rates $\langle\Gamma_N\rangle$ and $\langle\Gamma_U\rangle$, together with the ratio $\langle\Gamma_N\rangle/\langle\Gamma_U\rangle$, for the 1-nm-wide AGNR. (g,h) Corresponding frequency-dependent N and U scattering rates in the 1-nm-wide Cove-GNR at 100 and 300 K, respectively. (i) Transport-weighted average scattering rates and their ratio for the 1-nm-wide Cove-GNR.

namics, phonon Monte Carlo simulations, lattice dynamics, and full-LBTE calculations based on the same NEP-GNRs potential. Cove-GNRs exhibit lower thermal conductivity than pristine AGNRs across the length and width ranges considered. The MD–MC comparison shows that geometric boundary reflection captures only part of this reduction. The model residual is largest at short lengths and small widths, whereas the boundary contribution becomes relatively more important as either dimension increases.

Participation-ratio and real-space eigenvector analyses show that the cove geometry changes the vibrational eigenstates and introduces partially confined and strongly edge-confined modes in the low- and intermediate-frequency ranges. These modal features are absent from the semiclassical MC model, although the MD–MC residual cannot be assigned to a single microscopic mechanism.

Cove-GNRs also exhibit a smaller full-LBTE correction to the RTA result and a lower transport-weighted $\langle\Gamma_N\rangle/\langle\Gamma_U\rangle$ ratio. The two trends indicate a reduced role of momentum-conserving mode coupling and a greater relative importance of resistive momentum relaxation. Cove-edge patterning therefore changes both finite-size thermal transport and the intrinsic scattering balance of the nanoribbon.

Data availability

The processed data supporting the findings of this study are available from the corresponding authors upon reasonable request.

CRediT authorship contribution statement

Fei Yin: Validation, Formal analysis, Investigation,

Writing - original draft. **Gang Wang:** Validation, Formal analysis, Investigation, Writing - original draft. **Alexander A. Barinov:** Formal analysis, Writing - review & editing. **Shixian Liu:** Conceptualization, Methodology, Validation, Formal analysis, Investigation, Writing - review & editing. **Ke Xu:** Conceptualization, Methodology, Supervision, Writing - review & editing.

Declaration of Competing Interest

The authors declare that they have no known competing financial interests or personal relationships that could have appeared to influence the work reported in this paper.

ACKNOWLEDGMENTS

This work was supported by the Department of Science and Technology of Liaoning Province (No. 2025-BSLH-012) and Bohai University On-campus Doctoral Start-up Project Funding. S. Liu and F. Yin gratefully acknowledge financial support from the China Scholarship Council (No. 202308090243 for S. Liu and No. 202408090635 for F. Yin).

[1] Y.-W. Son, M. L. Cohen, and S. G. Louie, Half-metallic graphene nanoribbons, Nature **444**, 347 (2006).
[2] M. Y. Han, B. Özyilmaz, Y. Zhang, and P. Kim, Energy Band-Gap Engineering of Graphene Nanoribbons, Phys. Rev. Lett. **98**, 206805 (2007).
[3] H. Wang, H. S. Wang, C. Ma, L. Chen, C. Jiang, C. Chen, X. Xie, A.-P. Li, and X. Wang, Graphene nanoribbons for quantum electronics, Nat Rev Phys **3**, 791 (2021).
[4] A. K. Majee and Z. Aksamija, Length divergence of the lattice thermal conductivity in suspended graphene nanoribbons, Phys. Rev. B **93**, 235423 (2016).
[5] A. A. Balandin, S. Ghosh, W. Bao, I. Calizo, D. Teweldebrhan, F. Miao, and C. N. Lau, Superior Thermal Conductivity of Single-Layer Graphene, Nano Letters **8**, 902 (2008).
[6] L. Lindsay, D. A. Broido, and N. Mingo, Flexural phonons and thermal transport in graphene, Physical Review B **82**, 115427 (2010).
[7] S. Liu, F. Yin, and V. I. Khvesyuk, Investigating Anisotropic Three-Phonon Interactions in Graphene's Thermal Conductivity Using Monte Carlo Method, International Journal of Thermophysics **46**, 22 (2025).
[8] M. Batzill, The surface science of graphene: Metal interfaces, CVD synthesis, nanoribbons, chemical modifications, and defects, Surface Science Reports **67**, 83 (2012).
[9] Z. Aksamija and I. Knezevic, Lattice thermal conductivity of graphene nanoribbons: Anisotropy and edge roughness scattering, Applied Physics Letters **98**, 141919 (2011).
[10] W. J. Evans, L. Hu, and P. Keblinski, Thermal conductivity of graphene ribbons from equilibrium molecular dynamics: Effect of ribbon width, edge roughness, and hydrogen termination, Applied Physics Letters **96**, 203112 (2010).
[11] Y. Wang, B. Qiu, and X. Ruan, Edge effect on thermal transport in graphene nanoribbons: A phonon localization mechanism beyond edge roughness scattering, Applied Physics Letters **101**, 013101 (2012).
[12] X. Wan, D. Ma, D. Pan, L. Yang, and N. Yang, Optimizing thermal transport in graphene nanoribbon based on phonon resonance hybridization, Materials Today Physics **20**, 100445 (2021).
[13] H. Wei, Y. Hu, H. Bao, and X. Ruan, Quantifying the diverse wave effects in thermal transport of nanoporous graphene, Carbon **197**, 18 (2022).
[14] S. Liu, Z. Zong, F. Yin, V. Khvesyuk, and N. Yang, Quantifying particle and wave effects in phonon transport of pillared graphene nanoribbons, International Journal of Thermal Sciences **217**, 110067 (2025).
[15] S. Tian, T. Wang, H. Chen, D. Ma, and L. Zhang, Phonon coherent transport leads to an anomalous boundary effect on the thermal conductivity of a rough graphene nanoribbon, Physical Review Applied **21**, 064005 (2024).
[16] B. Liu, Z. Tian, A. A. Barinov, and M. Wang, Wave-like thermal phonons revealed by localization in graphene phononic crystals, Applied Physics Letters **128**, 112206 (2026).
[17] A. Cepellotti, G. Fugallo, L. Paulatto, M. Lazzeri, F. Mauri, and N. Marzari, Phonon hydrodynamics in two-dimensional materials, Nature Communications **6**, 6400 (2015).
[18] Y. Guo and M. Wang, Phonon hydrodynamics and its applications in nanoscale heat transport, Physics Reports **595**, 1 (2015).
[19] G. Chen, Non-Fourier phonon heat conduction at the microscale and nanoscale, Nature Reviews Physics **3**, 555 (2021).
[20] X. Sun, S. Lu, S. Shan, Z. Zhang, and J. Chen, Origin of superdiffusive thermal transport in one-dimensional van der Waals atomic chains, Physical Review B **111**, 205404 (2025).
[21] K. Xu, Y. Li, D. Ding, T. Liang, J. Wu, and J. Xu, Critical Size Transitions in Silicon Nanowires: Amorphization, Phonon Hydrodynamics, and Thermal Conductivity, The Journal of Physical Chemistry Letters **16**, 8580 (2025).
[22] Y. Machida, A. Subedi, K. Akiba, A. Miyake, M. Tokunaga, Y. Akahama, K. Izawa, and K. Behnia, Observation of Poiseuille flow of phonons in black phosphorus, Science Advances **4**, eaat3374 (2018).
[23] S. Huberman, R. A. Duncan, K. Chen, B. Song, V. Chiloyan, Z. Ding, A. A. Maznev, G. Chen, and K. A. Nelson, Observation of second sound in graphite at temperatures above 100 K, Science **364**, 375 (2019).
[24] J. Liu, B.-W. Li, Y.-Z. Tan, A. Giannakopoulos, C. Sanchez-Sanchez, D. Beljonne, P. Ruffieux, R. Fasel, X. Feng, and K. Müllen, Toward Cove-Edged Low Band Gap Graphene Nanoribbons, Journal of the American Chemical Society **137**, 6097 (2015).

[25] X. Wang, J. Ma, W. Zheng, S. Osella, N. Arisnabarreta, J. Droste, G. Serra, O. Ivasenko, A. Lucotti, D. Beljonne, M. Bonn, X. Liu, M. R. Hansen, M. Tommasini, S. De Feyter, J. Liu, H. I. Wang, and X. Feng, Cove-Edged Graphene Nanoribbons with Incorporation of Periodic Zigzag-Edge Segments, Journal of the American Chemical Society **144**, 228 (2022).

[26] K. Liu, W. Zheng, S. Osella, Z.-L. Qiu, S. Böckmann, W. Niu, L. Meingast, H. Komber, S. Obermann, R. Gillen, M. Bonn, M. R. Hansen, J. Maultzsch, H. I. Wang, J. Ma, and X. Feng, Cove-Edged Chiral Graphene Nanoribbons with Chirality-Dependent Bandgap and Carrier Mobility, Journal of the American Chemical Society **146**, 1026 (2024).

[27] T. J. Sisto, Y. Zhong, B. Zhang, M. T. Trinh, K. Miyata, X. Zhong, X.-Y. Zhu, M. L. Steigerwald, F. Ng, and C. Nuckolls, Long, Atomically Precise Donor–Acceptor Cove-Edge Nanoribbons as Electron Acceptors, Journal of the American Chemical Society **139**, 5648 (2017).

[28] M. Omini and A. Sparavigna, An iterative approach to the phonon Boltzmann equation in the theory of thermal conductivity, Physica B: Condensed Matter **212**, 101 (1995).

[29] W. Li, J. Carrete, N. A. Katcho, and N. Mingo, ShengBTE: A solver of the Boltzmann transport equation for phonons, Computer Physics Communications **185**, 1747 (2014).

[30] A. Togo, First-principles Phonon Calculations with Phonopy and Phono3py, Journal of the Physical Society of Japan **92**, 012001 (2023).

[31] S. Liu, G. Zhang, F. Yin, A. A. Barinov, V. I. Khvesyuk, and N. Yang, Temperature dependence of specific heat capacity of nanostructures via neuroevolution machine-learned potential, Journal of Applied Physics **138**, 104301 (2025).

[32] F. Yin, S. Liu, Y. Dong, A. A. Barinov, K. Xu, and V. I. Khvesyuk, Accelerated phonon transport calculations for nanostructures: Combining neuroevolution potentials and compressed sensing, Journal of Applied Physics **139**, 135103 (2026).

[33] Z. Fan, Z. Zeng, C. Zhang, Y. Wang, K. Song, H. Dong, Y. Chen, and T. Ala-Nissila, Neuroevolution machine learning potentials: Combining high accuracy and low cost in atomistic simulations and application to heat transport, Physical Review B **104**, 104309 (2021).

[34] Z. Fan, Improving the accuracy of the neuroevolution machine learning potential for multi-component systems, Journal of Physics: Condensed Matter **34**, 125902 (2022).

[35] T. Liang, K. Xu, E. Lindgren, Z. Chen, R. Zhao, J. Liu, E. Berger, B. Tang, B. Zhang, Y. Wang, K. Song, P. Ying, N. Xu, H. Dong, S. Chen, P. Erhart, Z. Fan, T. Ala-Nissila, and J. Xu, Nep89: Universal neuroevolution potential for inorganic and organic materials across 89 elements (2025), arXiv:2504.21286 [cond-mat.mtrl-sci].

[36] Y. Wang, Z. Fan, P. Qian, M. A. Caro, and T. Ala-Nissila, Density dependence of thermal conductivity in nanoporous and amorphous carbon with machine-learned molecular dynamics, Physical Review B **111**, 094205 (2025).

[37] T. Liang, K. Xu, P. Ying, W. Jiang, M. Han, X. Wu, W. Ouyang, Y. Yao, X. Zeng, Z. Ye, Z. Fan, and J. Xu, Probing the ideal limit of interfacial thermal conductance in two-dimensional van der Waals heterostructures, npj Computational Materials **12**, 11 (2026).

[38] L. Chaput, Direct Solution to the Linearized Phonon Boltzmann Equation, Physical Review Letters **110**, 265506 (2013).

[39] N. Malviya and N. K. Ravichandran, Indicators for phonon hydrodynamics from first-principles predictions of thermal conductivity (2026), arXiv:2605.17947 [cond-mat.mtrl-sci].

[40] W. Cai, A. L. Moore, Y. Zhu, X. Li, S. Chen, L. Shi, and R. S. Ruoff, Thermal Transport in Suspended and Supported Monolayer Graphene Grown by Chemical Vapor Deposition, Nano Letters **10**, 1645 (2010).

[41] J.-U. Lee, D. Yoon, H. Kim, S. W. Lee, and H. Cheong, Thermal conductivity of suspended pristine graphene measured by Raman spectroscopy, Physical Review B **83**, 081419 (2011).

[42] S. Chen, A. L. Moore, W. Cai, J. W. Suk, J. An, C. Mishra, C. Amos, C. W. Magnuson, J. Kang, L. Shi, and R. S. Ruoff, Raman Measurements of Thermal Transport in Suspended Monolayer Graphene of Variable Sizes in Vacuum and Gaseous Environments, ACS Nano **5**, 321 (2011).

[43] X. Xu, L. F. C. Pereira, Y. Wang, J. Wu, K. Zhang, X. Zhao, S. Bae, C. T. Bui, R. Xie, J. T. L. Thong, B. H. Hong, K. P. Loh, D. Donadio, B. Li, and B. Özyilmaz, Length-dependent thermal conductivity in suspended single-layer graphene, Nature Communications **5**, 3689 (2014).